Plasmon 3D Electron Tomography and Local Electric-field Enhancement of Engineered Plasmonic Nano-antennas

B. S. Archanjo[1,2], T. L. Vasconcelos[1], B. S. Oliveira[1], C. Song[2], F. Allen[2,3], C. A. Achete[1], P. Ercius[2]

1 Divisao de Metrologia de Materiais, Instituto Nacional de Metrologia, Qualidade e Tecnologia (INMETRO), Duque de Caxias, RJ 25250-020, Brazil

2 National Center for Electron Microscopy, Molecular Foundry, Lawrence Berkeley National Laboratory, 1 Cyclotron Rd., Berkeley, California 94720, United States

3 Department of Materials Science and Engineering, University of California, Berkeley, 210 Hearst Ave., Berkeley, California 94720, United States

Abstract

Plasmonic nano-antennas are pushing the limits of optical imaging resolution capabilities in near-field scanning optical microscopy (NSOM). Accordingly, these techniques are driving the basic understanding of photonic and optoelectronic nanoscale devices with applications in sensing, energy conversion, solid-state lighting and information technology. Imaging the localized surface plasmon resonance (LSPR) at the nanoscale is a key to understanding the optical responses of a given tip geometry in order to engineer better plasmonic nano-antennas for near-field experiments. In recent years the advancement of focused ion beam technology provides the ability to directly modify plasmonic structures with nanometer resolution. Also, scanning transmission electron microscopy (STEM) with electron energy loss spectroscopy (EELS) is an established technique allowing imaging of LSPR. Specifically, the combination of these two techniques provides spectrally sensitive two-dimensional (2D) imaging information to better visualize and understand LSPR on the nanometer scale. This can be combined with electron tomography to provide the three-dimensional LSPR distribution. Here we demonstrate the fabrication of Au nano-pyramids using helium ion microscopy, and analyze the LSPR in 3D reconstructions produced by total variation (TV)-norm minimization of a set of 2D STEM-EELS maps. Additionally, a boundary element simulation method was used to verify the experimentally observed nanopyramid LSPR modes. Finally, we show that the point-spread-functions (PSF) of LSPR mode hot spots in nanopyramids differ to local electric-field enhancement under optical excitation making direct comparison to NSOM experimental resolution difficult. However, the STEM-EELS results show how LSPR modes are influenced by the tip characteristics, which can inform the development of new nano-antenna designs.

Keywords

Surface Plasmon, EELS, Tomography, Nano-Antennas, NSOM, Nanofabrication

Introduction

Optical near-field imaging systems generate spatial resolution far beyond the optical diffraction limit. In this sense, optical near-field systems provide revolutionary capabilities for the field of nanotechnology, allowing the use of optical techniques to characterize nanoscale objects at high spatial resolution[1-5]. A few experiments demonstrated tens of nanometers resolution[6-9] and impressive sub-nanometer resolution was already achieved in ultra-high vacuum[10]. Subwavelength spatial resolution is reached by holding a sharp metal tip a few nanometers above the sample surface – which provides for both illumination and collection – to make use of the evanescent wave components of the light scattered from the sample (the near-field optical information)[11]. In order to do so, the tip should generate a high field enhancement localized at the vicinity of the tip apex. Therefore, the key to improve and control the tip's optical efficiency, necessary to provide high contrast near-field/far-field images, is to use the intense, localized field enhancement typical of localized surface plasmon resonance (LSPR) modes[1]. However, to date most optical near-field experiments dependent heavily on the specific LSPR behavior of a particular nano-antenna, which are not completely understood and difficult to replicate[1]. Development of techniques that can measure and predict the plasmonic response of new nano-antenna designs is needed[12].

In recent years many studies have tried to improve optical near-field imaging resolution and efficiency by constructing nanopyramids able to support LSPR, so-called plasmonic nano-antenna engineering. Different shapes, materials, fabrication techniques, experimental setups and theoretical approaches have been used to understand, control and improve resolution and reproducibility of optical near field techniques[1-3, 13]. Recently developed computer simulations of the plasmonic behavior of objects at the submicrometer- and nano-scale utilize the metal nanoparticle boundary element method (MNPBEM)[14-16]. The MNPBEM method solves Maxwell's equations for a dielectric environment and simulates EELS spectra as well as local field enhancement under plane wave excitation (usually used as optical excitation). Such a theoretical framework allows researchers to test the plasmonic response of a particular tip design before fabrication. We used the retarded simulations of the full Maxwell's equations approach (without the quasistatic approximation) of MNPBEM which is suitable for extended plasmonic structures in the size range of the ones investigated here Also, other recent numerical approaches that solve the inverse problem can be found in the literature[17], however it goes beyond the scope of this work. Then, nano-scale fabrication of a candidate plasmonic nano-antenna as defined by numerical simulations can be realized using focused ion beam (FIB) technology. Recently, helium ion microscopy (HIM) has proven to be an excellent technique to produce high quality nanoscale devices including a few nano-antennas [18-22]. Finally, electron energy loss spectroscopy (EELS) acquired by scanning transmission electron microscopy (STEM) can reveal the complicated connection between metal nano-object shapes and their LSPR behavior with nanometer spatial resolution and ~100 meV energy resolution [1, 23-24].

Still, STEM-EELS measurements are only 2D projections of the full 3D plasmonic tip response, which is an important measure of quality for optical near-field imaging experiments. It is therefore desired to acquire 2D STEM-EELS maps at different viewing angles and reconstruct the 3D plasmonic response by electron tomography. STEM-EELS is a relatively time-consuming and dose-intensive measurement technique and can only be used to take a limited number of tilt angles. To test the achievable resolution using limited tilts for the LSPR 3D tomography, we have compared the performance of the conventional methods, namely, filtered back projection (FBP)[25] and simultaneous iterative reconstruction technique (SIRT)[25] and also an advanced method based on total variation (TV)-norm minimization also commonly referred to as compress sensing (CS)[26]. TV-minimization was previously used to produce high-fidelity LSPR 3D tomography reconstructions of a silver nanocube with relatively few measurements[27]. In this work, we also utilized TV-minimization to deal with the missing information in 2D STEM-EELS maps due to absorption and multiple-scattering in the thick bulk regions of our nanopyramids (see methods for more details).

As reported by a few works[28-31], LSPR modes mapped via STEM-EELS do not directly reflect the local electric-field enhancement because EELS measurements include losses due to radiation emission and absorption in the tip[32]. In STEM-EELS, the electron beam is used to both excite and measure, and then EELS reflects the magnitude of the induced electric field at the location of the sub-nanometer electron beam. It is also claimed that no qualitative difference is observed between STEM-EELS maps of LSPR modes and electric field enhancement for particles with edges and corners[28]. Further, most work in correlating STEM-EELS and LSPR has been done on nanoparticles or flat metal patterns. We discuss correlations between LSPR mode maps from EELS and the spatial distribution of local field enhancement from simulation for application in engineered nanopyramid plasmonic antennas.

In order to improve our understanding of and the performance of engineered plasmonic nano-antennas, this work focuses on the following topics:

1 - Nanopyramids designed via computational simulation and fabricated by chemical etching, coarse milled by Ga^+ focused ion beam (FIB) and fine milled by HIM.

2 - LSPR 3D tomography from STEM-EELS maps via tomographic reconstruction using total variation (TV-) minimization, SIRT and FBP.

3 - Correlation of the 3D PSF calculated from the LSPR optical modes of nanopyramids with simulated local electric-field enhancement under plane wave optical excitation.

Results and discussions

The LSPR phenomenon is based on confinement of the electron cloud in a sub-wavelength sized object, where the resonance is achieved by matching the feature size with the wavelength of the free electron gas oscillation. Thus, confinement of plasmons

in a nanopyramid is suitable for a local field enhancement at the apex. Fig. 1a shows a HIM image of the fabricated Au nanopyramid with a notch near the apex to define a feature of known size to confine the plasmonic oscillations. Fig. 1b shows the simulated (top, black) and experimental (bottom, blue) EELS spectra for a focused 300 kV electron beam positioned near the nanopyramid apex as indicated by the asterisks in Fig. 1c (see methods for details). Fig. 1c displays (left) an experimental high-angle annular dark field (HAADF-) STEM image of the nanopyramid showing its overall shape and (right) a surface mesh of the corresponding simulated nanopyramid structure used in a MNPBEM simulation (see methods for details of the simulations). Three absorption peaks are observed in the experimental EELS spectrum as well as in the numerically simulated spectrum. The less intense experimental EELS peak at around 2.3 eV is attributed to absorption related to interband transitions connecting upper energy states in the 5d valence band with unoccupied states in the half-filled hybrid 6sp band for gold[1, 33]. The other two strong peaks, at 1.1 eV and 1.8 eV in the experimental EELS data and 1.3 and 1.9 eV in the numerically simulated data, are LSPR peaks. The relatively small discrepancy in energy between simulated and experimental data is discussed later in this text.

Using STEM-EELS mapping, we acquire spectra using a sub-nanometer sized focused electron beam at a series of positions in a 2D grid from nanometer-scale regions outside the nanopyramid tip in the so-called aloof geometry. The incoming aloof electron beam excites surface plasmons within approximately a 10 nanometer radius limited by spatial delocalization of these transitions[23]. By summing the intensity under each peak identified in Fig. 1b at every 2D beam position we create a map of the plasmon energy loss. Simulated plasmon absorption maps (Fig. 1d right) allow us to assign the less energetic peak as the first LSPR (two hot spots at the nanopyramid apex and notch position) and the more energetic peak as the second LSPR mode (three hot spots). The EELS signal can only be collected outside the nanopyramid since the electron beam is strongly scattered when passing through the bulk part of the Au tip. However, the MNPBEM numerical simulations only account for electromagnetic interactions between the electron beam and the object material. Thus, the electron collisions with Au atomic nuclei are not included allowing the simulation of EELS spectra from the bulk of the nanopyramid. For a better visual comparison between experiment and simulation, the simulated maps in Fig. 1d had the data removed where the electron beam passes through the nanopyramid. For simulated maps with all data see Fig. S1. We have also simulated a floating nanopyramid without the neck produced during the HIM grooving, which we called the ideal shape in Fig. S1. However, no important differences were observed when comparing the ideal and experimental nanopyramid geometries.

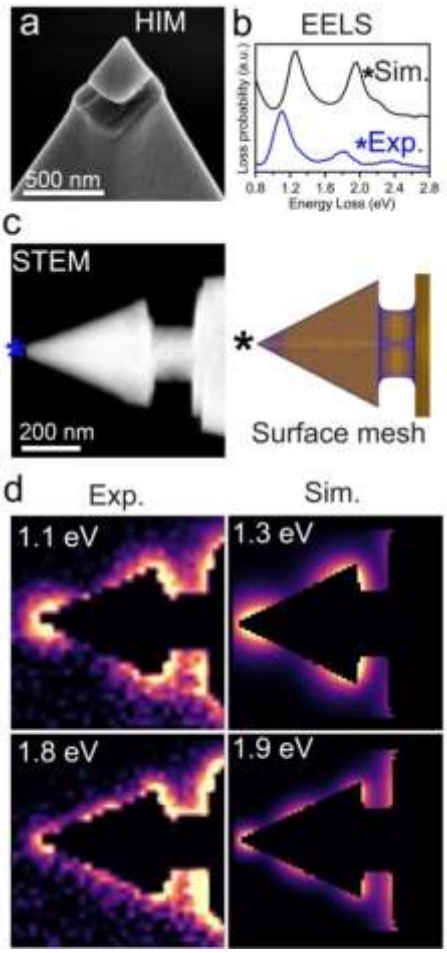

Fig.1 - STEM–EELS spectrum imaging and MNPBEM simulation of a gold nanopyramid. (a) HIM image of the gold nanopyramid. (b) Experimental and simulated EELS spectra from the apex of the gold nanopyramid. (c) Experimental HAADF-STEM image (left). Surface mesh used in MNPBEM simulation (right). (d) Experimental and simulated EELS maps (same scale as in c) of the two strong LSPR modes observed at the nanopyramid apex (as shown in b). See also Figs. S1 and S2. Supplementary Video 1 shows the 2D EELS maps at all energies from 0.8 to 2.4 eV in 0.1 eV steps.

Determining a scaling relation connecting the nanopyramid morphology and the wavelength of the incident (or scattered) radiation field to promote LSPR excitation is crucial for designing optically efficient near-field tips[1, 34]. However, fabricating nano-antennas of many geometries is challenging and time consuming. Therefore, simulation was used to understand the influence of tip geometry on the effects of near field enhancement and then validated with fewer experiments. As corresponding metrics between simulation and experiments, we explored the influence of the pyramid opening angle θ and lateral length L (distance between apex and base vertices; see inset to Fig. 2) on the LSPR energy E_{LSPR} and the equivalent radiation field wavelength λ_{LSPR}. Therefore, both nanopyramid geometric parameters (L, θ) can be varied to match the LSPR energy mode to the desired wavelength of a near-field optical imaging system.

Fig. 2 shows a plot of L for nanopyramids with different θ (colored by angle) as a function of the λ_{LSPR} for first (▲), second (●) and third (■) LSPR modes. The larger gray symbols represent the experimental STEM-EELS data collected from three different nanopyramids. See Fig. S3 and Supplementary Video 2 for the full experimental data. The smaller symbols connected by solid lines are extracted from MNPBEM numerical simulations of 21 nanopyramids with different opening angles distinguished by different colors and lengths (L). For the analysis below, we refer to mode 1 (lowest E_{LSPR}), mode 2 and mode 3 (highest E_{LSPR}) rather than the associated energy channels for more easy comparison between simulated and experimental data.

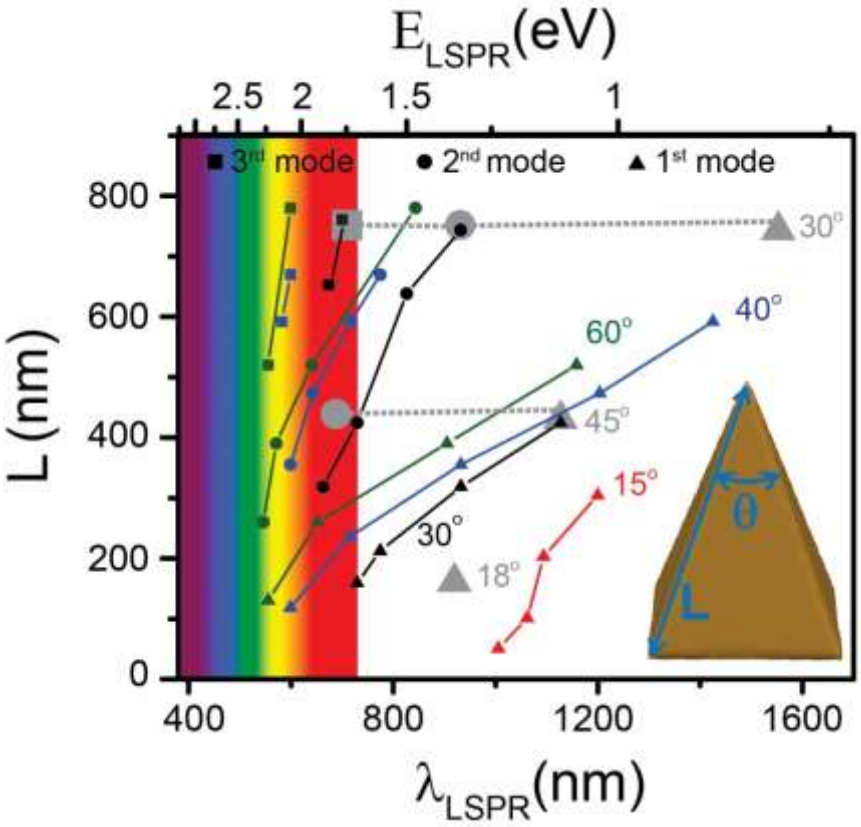

Fig. 2 – Scaling relations showing the nanopyramid lateral length L against the equivalent optical LSPR wavelength λ_{LSPR} (according to LSPR energy E_{LSPR}) for nanopyramids having different opening angles θ. The symbols indicate 1st (triangles), 2nd (circles), and 3rd (squares) modes respectively. The colors indicate for the nanopyramid opening angle 15° (red), 30° (black), 40° (blue) and 60° (green) for the simulated data. The gray symbols connected by dashed lines represent the experimental results (EELS) from three different nanopyramids of L = 160 nm, 450 nm and 750 nm and opening angles of 18°, 45° and 30° respectively. The visible light range is background colored with the respective electromagnetic spectrum color as a guide for the eyes. The nanopyramid images, EELS spectra and maps can be seen in Fig. S3. Supplementary Video 2 shows the 2D EELS maps from 0.8 up to 2.4 eV for the experimental EELS data of the three experimental nanopyramids. Table S1 summarizes the results of the numerical simulations.

In general, optical nano-antennas compatible with the visible electromagnetic spectrum (indicated as a rainbow background in Fig. 2) are more desirable, since photons within this energy range interact with matter through transitions of electronic states spatially confined on the nanoscale which can, for instance, be used for local photoluminescence[35] and Raman measurements[11]. However, in this regime metals do not behave as a perfect metal and the conventional antenna theory fails, requiring simulation (MNPBEM) and experimental (EELS) development to design highly efficient nano-antennas[36]. Then as a first interesting result, Fig. 2 shows that only nanopyramids with $\theta > 30°$ and with L < 300 nm will exhibit a 1st LSPR mode in the visible electromagnetic spectrum. This restricts the parameter range for tip fabrication. Looking for other modes, nanopyramids with L between 250 nm and 600 nm will show the 2nd LSPR mode in the visible range ($40^o < \theta < 60^o$), whereas nanopyramids larger than 600 nm and smaller than 800 nm, the largest nanopyramid simulated here, will show the 3rd LSPR mode in the visible range. Remarkably, nanopyramids with L ~ 300 nm will have 1st and the 2nd LSPR modes in the optical range, and nanopyramids with $\theta > 40°$ and having 450 nm < L < 600 nm will have the 2nd and the 3rd LSPR modes as well as in the optical range, thus being suitable for near-field experiments using the corresponding optical laser wavelengths. It is worth noting that nanopyramids with small opening angles, of ~15 only exhibit LSPR modes positioned in the mid-infrared spectrum region. These conclusions are summarized in the Table S1 in the supporting information, The lower gray triangle in Fig. 2 represents the EELS data from a nanopyramid with $\theta = 18°$ and L=170 nm presenting a single LSPR mode at 920 nm (1.35 eV), which reasonably agrees with the simulated results for nanopyramids with $\theta = 15°$ (red curve in Fig. 2).

The absence of LSPR modes in the visible spectrum range at the apex of nanopyramids having small ($< 15^o$) opening angles agrees with previous results published for conical tips[37]. Although the authors do not call attention to this occurrence, their data indicates that conical tapers having $\theta < 15°$ do not show surface plasmon absorption above 1.8 eV, whereas a conical tip with $\theta = 47°$ shows surface plasmon absorptions up to 2.3 eV, similar to what we observe here with nanopyramid tapers.

The MNPBEM numerical simulations showed good agreement with the experimental results, and only small energy shifts of 0.1 to 0.2 eV are observed. This small energy discordance may be assigned to some gold surface flaws generated by HIM patterning (amorphization and redeposition of gold), an extra surface layer of carbon contamination, or morphology details (surface roughness) not accounted for in the simulated nanopyramids. Other such studies have reported energy shifts between experiment and simulation as high as 0.7 eV attributed to factors in the very local environment[38] including roundness of the edge structure[39], retardation effects[27], and parametrization of the dielectric function[27].

Having determined the validity of our simulations with experimental 2D STEM-EELS maps, we want to additionally validate and understand the plasmon delocalization in

three-dimensions in order to predict how the tip geometry will impact the resolution of scanned near-field optical images. 2D maps will only show the projected plasmon loss along a certain viewing direction, however the actual 3D shape of the plasmon loss can be obscured by overlap of features along the projection direction especially for non-isotropic shapes. Determining the full 3D shape requires acquiring 2D STEM-EELS maps at a series of viewing angles, and then reconstructing the 3D plasmon-loss using electron tomography. 3D reconstruction will provide information if a given LSPR hot spot is located at the edges, corners or faces of the nano-antenna to further validate the agreement between simulation and experiment. The main limitations in performing 3D tomography reconstruction from STEM-EELS maps of optical nanopyramids are the extremely high electron scattering of the constituent materials (typically Au or Ag), the thickness of the bulk portion of the plasmonic structure, and the long acquisition time required to collect each projection. Typically, an experiment might take a few hours for collecting 5-10 projections, and although Au is very stable for high electron beam dose, C deposition is often observed. Therefore, only a few STEM-EELS projections can realistically be collected for 3D tomography. As already mentioned here, the highly scattering material together with the sample thickness (easily > 100 nm) do not allow the collection of EELS data from inside the sample. Thus, the STEM-EELS maps are missing information from inside the bulk structure and are not true projections of the plasmon loss at every point in the structure as required by electron tomography. We compare reconstructions of full simulated, masked simulated and experimental data to show how well experiments compare to the expected 3D distribution despite this missing data. For those interested in the details of the 3D reconstruction please see methods and Fig. S4 where simulated sinograms, containing full and missing information, can be compared to a sinogram of experimental STEM-EELS projections.

In this work we used the experimental and simulated surface plasmon maps at different angles as the input to three tomographic reconstruction methods: SIRT, FBP[25] and nonlinear image reconstruction by TV-minimization (also known as compressed sensing)[27, 40-42]. The TV-minimization algorithm has already proven to yield representative electron tomography reconstructions with fewer tilt-angles than conventional reconstruction algorithms. Under certain assumptions it works especially well for plasmon maps with large, smooth features [26-27, 43]. Here the performance of SIRT, FBP and TV-minimization algorithms are compared using very few projections, and without the missing information from inside the bulk material. Further details of the reconstruction process can be found in the Methods. In Fig. S5 two perpendicular slices from each reconstruction of the first LSPR mode are plotted using the three reconstruction methods for full (unmasked) simulated data, masked simulated data and experimental data. For the full simulated data, SIRT presents the best reconstruction fidelity and closest match to the input projections where the LSPR modes are concentrated at the nanopyramid corners; however, FBP and TV-minimization show significant high plasmon signal inside the nanopyramid which do not agree with the full simulated projections. An understanding of why this occurs is beyond the scope of this paper. We therefore consider the SIRT reconstruction of the full simulated data close to

the expected 3D plasmon loss distribution. On the other hand, for the masked simulated data and experimental data, TV-minimization seems to produce a better fidelity reconstruction. See Fig. S6 for calculated projections from SIRT and TV-minimization reconstruction of full and masked simulated data. Here we used discrete wavelet transforms (see methods) to provide the sparse representation of the transformed data. This transform is known to correctly handle smooth and piecewise smooth signals[26], including non-periodic steps, which is the case for the (internal) missing information in the masked simulated and experimental data. Lastly, the lack of information from inside the pyramid makes the data sparser in the wavelet domain, which possibly explains why the TV-minimization does not work well for the full unmasked data. In comparison, the reconstructed slices from SIRT and FBP have many artifacts due to the missing information from inside the bulk Au sample. In Fig. 3, 3D volume renderings of experimental data using the TV-minimization algorithm is compared with the SIRT reconstruction from the full simulated data for the first two modes. The supplementary Video 3 shows the animated 3D visualization of these two LSPR modes.

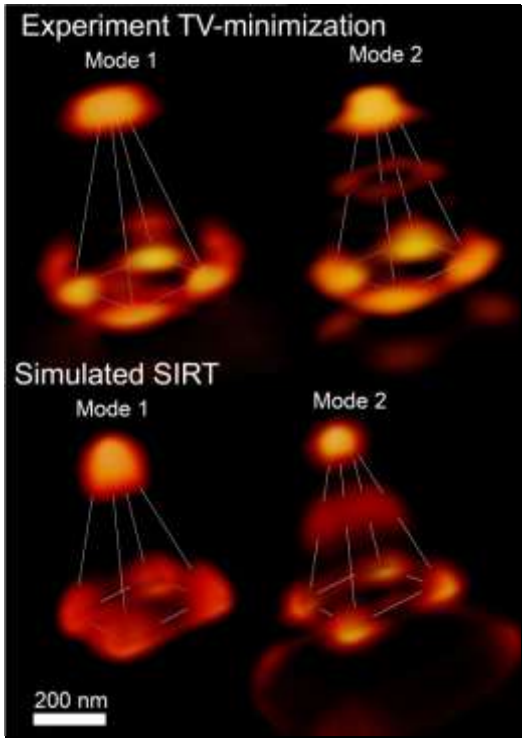

Fig. 3 – 3D volume rendering of the LSPR components of an Au nanopyramid reconstructed by different methods. Here the best 3D tomography reconstructions can be compared, namely, TV-minimization for experimental data and SIRT when the full, unmasked simulated data is used. See supplementary Video 3 for animated 3D visualization.

The 3D reconstruction provides direct spatial information about the LSPR hotspot at the nanopyramid apex, thus allowing the estimation of the PSF (which we can compare to the optical image resolution) of the LSPR modes studied here. The results of the PSF estimation as measured by a fit to a 3D Gaussian to the reconstructed intensity at the apex is presented in Table 1. One can note a reasonable agreement between

experimental and simulated values. We note that the calculated FWHMs in the X-Y direction are in the range of 110 to 150 nm, which is larger than reported spatial resolution in near-field microscopy experiments using similar shaped tips (usually cone-like tips)[1, 6, 10]. The reason for this difference lies on the short range effect of optical field enhancement produced by a tip supporting LSPR under optical excitation, whereas in an EELS experiment the loss probability of LSPR excitation represents the magnitude of the electron-induced electric field at the location of the electron beam. In order to confirm this observation we have made a simulation using plane wave excitation with MNPBEM of a tip with similar parameters as shown in Fig. 4a. Fig. 4b compares the profiles of EELS-LSPR signals and local field enhancement located a few nanometers away from the tip (10 to 20 nm in the simulated and experimental EELS-LSPR and about 5 nm in the plane wave excitation simulation). The simulated and experimental STEM-EELS signals are much broader than the local field enhancement as previously determined in the literature for flat metal nanoparticles[30]. As a matter of comparison, we also simulated the field enhancement near a nanopyramid apex for different energies and compared this to STEM-EELS loss probability (spectra). A good agreement is observed mainly for the second mode in the visible range of the electromagnetic radiation. See Fig. S7 in the supporting information.

Table 1 also shows that the hot spot center of the LSPR modes at the nanopyramid apex is displaced to the internal part of the nanopyramid by about 30-60 nm, as also seen elsewhere for nanowires [44]. In addition, the FWHM in the Z direction (the nanopyramid axis) is smaller than the FWHM in the X-Y direction. This LSPR mode displacement and the smaller FHWM might explain the need for the tip to be very close to the surface in optical near-field experiments. In order to have enough field enhancement the taper apex must be very near to the sample surface, usually this distance is less than 10 nm.

This is an ongoing project and our methodology is being used in the development of different tip geometries including highly reproducible microfabricated nanopyramids with good optical characteristics. Although STEM-EELS does not exactly match the expected near-field resolution, we can find significant differences between the PSF from different LSPR modes and spatial direction (Z axis and XY plane). It has been shown that STEM-EELS is useful for such qualitative measurements of LSPR modes[28, 30]. In general, it looks like higher LSPR modes have smaller PSF in the 3 spatial directions. Our methodology can be used in the rational development of tips from different materials having different shapes and then compare the results using lasers tuned to their respective LSRP modes energy. Therefore, we will be able to better correlate STEM-EELS to local field enhancement and finally scanned near-field image resolution. This will improve our understanding of near-field experiments and will guide us to new nano-antenna designs.

Table 1 – Calculated 3D PSF of the experimental and full simulated EELS-LSPR modes.

LSPR mode	FWHM (nm)			Z displacement (nm)
	Z	X	Y	
Experiment (TV-minimization)				
mode 1	60±30	130±60	130±60	40
mode2	70±30	110±50	110±50	30
Simulated (SIRT)				
mode 1	130±60	150±70	150±70	60
mode 2	70±30	90±40	90±40	30

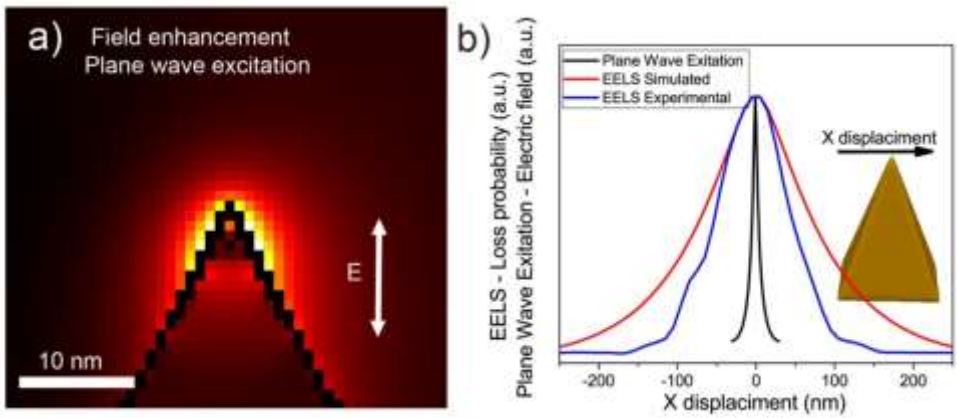

Fig. 4 – Optical excitation compared to STEM-EELS at the apex of a nanopyramid. a) Slice 2D map of the field enhancement (using a heat color map) calculated using plane wave excitation with MNPBEM. The electric-field vector is along the nanopyramid axis. b) The graph shows the profiles of the simulated (red) and experimental (blue) electron energy loss probability and the electric field (black) normalized to their peak values, for the LSPR mode 2 in the visible range. The electric-field enhancement is much more confined than the electron loss probability. See Fig. S7 in the supporting information for the comparison between field enhancement and EELS probability for different energies.

Conclusions

In summary we have compared the plasmon response of computationally simulated and focused ion-beam fabricated nanopyramids for optical near-field experiments. Our experimental STEM-EELS and simulated results based on boundary element methods match well providing a scaling relation to produce high quality near-field tips having LSPR modes optimized for the visible spectrum. In our analyses, we utilized a TV-minimization (compress sensing) electron tomography reconstruction method to produce 3D reconstructions of LSPR from STEM-EELS plasmon-loss maps. Notably,

by using TV-minimization the effect of missing information in the STEM-EELS maps due to the bulk of a highly-scattering, thick gold nanopyramid was minimized. Finally, the reconstructed data were used to extract the 3D PSF of the LSPR optical modes at the apex of the nanopyramid and compared to the calculated local electric-field enhancement under optical excitation. This PSF and achievable near-field optical experimental resolution differ by orders of magnitude. This is the first time this discrepancy in the spatial extent of these two quantities are demonstrated and it might be related to intrinsic differences between electron and photon excitation of LSRP modes of nano-objects. Our results indicate that STEM-EELS must be used with caution when directly describing photonic properties of engineered nano-antennas. This is an ongoing project where more research is being done to correlate STEM-EELS, local field enhancement calculations and near-field resolution. We will continue to improve our understanding of LSPR behavior with direct benefits to the development of new nano-antenna designs for NSOM.

Acknowledgments

B.S.A acknowledges the financial support from Faperj and CNPq through the program Science Without Borders under Grant 234217/2014-6. Work at the Molecular Foundry was supported by the Office of Science, Office of Basic Energy Sciences, of the U.S. Department of Energy under Contract No. DE-AC02-05CH11231. B.S.A. thanks Dr. John Turner and Dr. Mary Scott for helping with Ga FIB manipulation. B.S.A. also thanks Jihan Zhou for helping with AFM tips transfer setup used as tentative experiment in this work.

Methods

MNPBEM simulation. Boundary element method simulations were performed using the open-source MNPBEM Matlab Tolbox[14-15]. The gold dielectric function was taken from elsewhere[45]. Simulations of 2D EELS projections were calculated from 0° to 45° with 5° steps. The mesh used for simulations used an element area of ~10 nm^2 in the nanopyramid body with a refine function at the nanopyramid corners forcing the element area to increase from 5 nm^2 up to 10 nm^2. The gold wire body had a total size ~2 μm, the maximum element area used in the base of the gold wire body was about 50 nm^2 and the lateral of the gold wire were divided in 60 stripes. The nanopyramid and gold wire body had a total of 13000 surface elements. Retarded simulations which solve the full Maxwell equations, curved particle boundaries, 20 (2) integration points for diagonal (off-diagonal) Green function elements and 2 Å electron beam width were other used options. Plane wave excitation method was used for the local field enhancement calculation shown in Fig. 4. The electric-field has its direction set perpendicular to the nanopyramid base which is similar to near optical experiments already reported.

Electrochemical Etching of Gold Tips. Conical shaped gold tips were produced by the lamella-drop off electrochemical etching method[46]. For that we used 100 μm thick gold

wire with 99.995% purity, and a 37% HCl solution. For good reproducibility, automated control of the cathode current is required to interrupt the etching process when the tip is formed. After the etching process is complete, scanning electron microscopy (SEM) was used to select tips with apex diameters smaller than 50 nm, and open angles greater than 20°[1]. The wire is then attached to a TEM Cu grid using EPO-TEK® H22 conductive epoxy. See Fig. S8 for a scanning electron microscopy (SEM) images.

FIB coarse fabrication. The FIB milling processes were performed using a FEI Strata 235 dual beam at the National Center for Electron Microscopy facility of the Molecular Foundry (NCEM@MF). The accelerating voltage and ion current were set to 30 kV and 0.1 nA, respectively, generating the pyramid facets with ~15 μm in length. The gold etched tip is positioned head up and rotated 90° for milling each facet. See Fig. S8 for SEM and HIM images.

HIM fine fabrication. The HIM milling processes were performed using a Zeiss Orion Nanofab at UC Berkeley. The accelerating voltage and ion current were set to 30 kV and 2 pA, respectively. Patterning squares of about 150 x 150 nm^2 at 10^{19} ions/cm^2 were used to open the gap and make the notch keeping the nanopyramid connected to the body of the gold wire. The TEM grid with the gold wire is laid down in the Al stub with the pyramid facet edge facing up, therefore 0° or 180° rotation plus 45° tilt allows seeing one or another pyramid side. Using rectangle milling application the nanopyramid notch was milled from the two pyramid sides. The pyramid facets were then further sharpened at ~1 μm near the apex. See Fig. S8 for a HIM image.

STEM-EELS data acquisition. The FEI TEAM I (located at NCEM@MF) was operated at 300kV in STEM mode with the monochromator in decelerating mode at an excitation of 1.5. The beam convergence semi-angle was about 30 mrad. The scan step size was 20 nm with dwell time of 100 ms. EELS spectra were recorded on a Gatan GIF Tridiem energy filter with a collection semi-angle of 25 mrad, dispersion of 0.01 eV per channel and vertical binning 1. The energy resolution calculated as the full-width at half-maximum of the ZLP of the EELS spectra was ~80 meV. The projections were acquired from -45° to 45° with 7.5° steps.

Spectral processing. Data were first read and grouped in a 4D data file having the following axes: X position, Y position, energy loss and projection. Then the preprocessing algorithm was developed in Matlab and is available online as supporting files under the name preTomography.m, it align the ZLP peaks of all spectra, create a kernel composed of the average ZLP peak using the scanning far corners where plasmon signal is negligible, perform the Richardson-Lucy deconvolution based on Egerton's script [47-48], improving the energy resolution from 80 meV down to 50 meV (see Fig. S9 in the supporting information). Then the plasmon maps were extracted by summing over an energy window of 0.2 eV width with 0.1 step in the 0.8-2.4 eV range. Cross-correlation was used to align the projections.

3D reconstruction. The total variation (TV)-norm minimization electron tomography reconstruction used the conjugate gradient descent algorithm[42] as described elsewhere[26-27, 43] and only a few trivial modifications were made here. Briefly, we first Fourier transform the projection images to obtain radial data in the Fourier domain. This data is then Fourier transformed in to the image domain using the non-uniform fast Fourier transform (NUFFT)[49]. For the sparsifying transform, a Coiflet wavelet transform with eight vanishing moments is implemented via the WAVELAB package[50]. The weight for TV penalty and transform L1 penalty were chosen by testing selected slices of the reconstruction and comparing with simulated results. As the final step, the four-fold symmetry of the nanopyramid along the rotation axe is imposed to the reconstructed data. The reconstruction was performed in MATLAB and the algorithm named TVElectronTomography.m used here is available as a supplementary file. SIRT and FBP 3D reconstruction were made using the open-source Python package for tomographic data processing and image reconstruction Tomopy[25]. For SIRT and FBP, the four fold symmetry of the nanopyramid along the rotation axis is imposed to the input data which greatly improved the 3D reconstruction removing the missing wedge issue. Finally the 3D visualization (figures and movies) were accomplished in Tomviz[51].

Author Contribution

B.S.A. and P.E. designed the experiment, performed the electron microscopy and made the data analyses and the 3D electron tomography reconstructions. B.S.A. also performed simulations. T.L.V. and B.S.O designed the experiment and provide the etched gold tips. C.S. performed the electron microscopy. All authors interpreted and discussed the experimental results and wrote and edited the manuscript.

Notes: The authors declare no competing financial interest.

Support information

Figure containing full information about EELS experiment and EELS simulation (Fig. S1). Image showing the mesh of the nanopyramid real shape with the notch and the gold wire body (Fig. S2). EELS spectra, STEM image and 2D EELS maps for the LSRP modes of the experimental data from the three nanopyramids used in Fig. 2 (Fig. S3). Simulated and experimental sinograms from a slice in the middle of the nanopyramid (Fig. S4). Single slices from the STEM-EELS 3D tomography reconstruction for the first LSRP mode using TV-minimization, SIRT and FBP algorithms (Fig. S5). Projections of the reconstructed simulated full and masked data sets to the simulated 2D EELS maps (Fig. S6). Simulated and experimental electron loss probability compared to simulated electric field enhancement (Fig. S7). Images of the gold tip after each step fabrication (Fig. S8) Richardson-Lucy deconvolution (Fig. S9). Summary of the results from numerical simulation in Fig. 2 (Table S1). (PDF) 2D EELS maps at all energies from 0.8 to 2.4 eV in 0.1 eV steps of Fig. 1 data (Video 1) and Fig. 2 data (Video 2). Animated 3D visualization of the EELS electron tomography. (Video 3). Matlab codes used in this work (Matlab code. Zip).

References:

(1) Vasconcelos, T. L.; Archanjo, B. S.; Fragneaud, B.; Oliveira, B. S.; Riikonen, J.; Li, C.; Ribeiro, D. S.; Rabelo, C.; Rodrigues, W. N.; Jorio, A.; Achete, C. A.; Cançado, L. G., Tuning Localized Surface Plasmon Resonance in Scanning Near-Field Optical Microscopy Probes. *ACS Nano* **2015**, *9*, 6297.

(2) Schmidt, D. A.; Kopf, I.; Brundermann, E., A matter of scale: from far-field microscopy to near-field nanoscopy. *Laser Photonics Rev.* **2012**, *6*, 296.

(3) Mauser, N.; Hartschuh, A., Tip-enhanced near-field optical microscopy. *Chem. Soc. Rev.* **2014**, *43*, 1248.

(4) Kawata, S.; Inouye, Y.; Verma, P., Plasmonics for near-field nano-imaging and superlensing. *Nat. Photonics* **2009**, *3*, 388.

(5) Koenderink, A. F.; Alù, A.; Polman, A., Nanophotonics: Shrinking light-based technology. *Science* **2015**, *348*, 516.

(6) Cançado, L. G.; Jorio, A.; Ismach, A.; Joselevich, E.; Hartschuh, A.; Novotny, L., Mechanism of Near-Field Raman Enhancement in One-Dimensional Systems. *Phys. Rev. Lett.* **2009**, *103*, 186101.

(7) Ogawa, Y.; Yuasa, Y.; Minami, F.; Oda, S., Tip-enhanced Raman mapping of a single Ge nanowire. *Appl. Phys. Lett.* **2011**, *99*, 053112.

(8) Ogletree, D. F.; Schuck, P. J.; Weber-Bargioni, A. F.; Borys, N. J.; Aloni, S.; Bao, W.; Barja, S.; Lee, J.; Melli, M.; Munechika, K.; Whitelam, S.; Wickenburg, S., Revealing Optical Properties of Reduced-Dimensionality Materials at Relevant Length Scales. *Adv. Mater.* **2015**, *27*, 5693.

(9) Wang, L.; Xu, X. G., Scattering-type scanning near-field optical microscopy with reconstruction of vertical interaction. *Nat. Commun.* **2015**, *6*, 8973.

(10) Zhang, R.; Zhang, Y.; Dong, Z. C.; Jiang, S.; Zhang, C.; Chen, L. G.; Zhang, L.; Liao, Y.; Aizpurua, J.; Luo, Y.; Yang, J. L.; Hou, J. G., Chemical mapping of a single molecule by plasmon-enhanced Raman scattering. *Nature* **2013**, *498*, 82.

(11) Nat PhysComputer Physics CommunicationsAngewandte Chemie-International EditionAbstracts of Papers, t. A. N. M., New Orleans, LA, United States, March 23-27, 2003Cançado, Luiz Gustavo; Hartschuh, A.; Novotny, L., Tip-enhanced Raman spectroscopy of carbon nanotubes. *J. Raman Spectrosc.* **2009**, *40*, 1420.

(12) Richard-Lacroix, M.; Zhang, Y.; Dong, Z.; Deckert, V., Mastering high resolution tip-enhanced Raman spectroscopy: towards a shift of perception. *Chem. Soc. Rev.* **2017**, *46*, 3922.

(13) Hartschuh, A., Tip-Enhanced Near-Field Optical Microscopy. *Angew. Chem. Int. Ed.* **2008**, *47*, 8178.

(14) Hohenester, U.; Trügler, A., MNPBEM – A Matlab toolbox for the simulation of plasmonic nanoparticles. *Comput. Phys. Commun.* **2012**, *183*, 370.

(15) Hohenester, U., Simulating electron energy loss spectroscopy with the MNPBEM toolbox. *Comput. Phys. Commun.* **2014**, *185*, 1177.

(16) Sun, W.; Boulais, E.; Hakobyan, Y.; Wang, W. L.; Guan, A.; Bathe, M.; Yin, P., Casting inorganic structures with DNA molds. *Science* **2014**, *346*.

(17) Hörl, A.; Haberfehlner, G.; Trügler, A.; Schmidt, F.-P.; Hohenester, U.; Kothleitner, G., Tomographic imaging of the photonic environment of plasmonic nanoparticles. *Nat. Commun.* **2017**, *8*, 37.

(18) Archanjo, B. S.; Fragneaud, B.; Cançado, L. G.; Winston, D.; Miao, F.; Achete, C. A.; Medeiros-Ribeiro, G., Graphene nanoribbon superlattices fabricated via He ion lithography. *Appl. Phys. Lett.* **2014**, *104*, 193114.

(19) Archanjo, B. S.; Barboza, A. P. M.; Neves, B. R. A.; Malard, L. M.; Ferreira, E. H. M.; Brant, J. C.; Alves, E. S.; Plentz, F.; Carozo, V.; Fragneaud, B.; Maciel, I. O.; Almeida, C. M.; Jorio, A.; Achete, C. A., The use of a Ga + focused ion beam to modify graphene for device applications. *Nanotechnology* **2012**, *23*, 255305.

(20) Kollmann, H.; Piao, X.; Esmann, M.; Becker, S. F.; Hou, D.; Huynh, C.; Kautschor, L.-O.; Bösker, G.; Vieker, H.; Beyer, A.; Gölzhäuser, A.; Park, N.; Vogelgesang, R.; Silies, M.; Lienau, C., Toward Plasmonics with Nanometer Precision: Nonlinear Optics of Helium-Ion Milled Gold Nanoantennas. *Nano Lett.* **2014**, *14*, 4778.
(21) Olivier, S.; Konstantins, J.; Ivan, S.; Christian, H.; Urs, S.; Gian-Luca, B., Helium focused ion beam fabricated plasmonic antennas with sub-5 nm gaps. *Nanotechnology* **2013**, *24*, 395301.
(22) Giuseppe, C.; Alexander, K.; Frances, I. A.; Scott, D.; Simone, S.; Edward, W.; Paul, L.; Keiko, M.; Stefano, C., Nanoimprint of a 3D structure on an optical fiber for light wavefront manipulation. *Nanotechnology* **2016**, *27*, 375301.
(23) Nelayah, J.; Kociak, M.; Stephan, O.; Garcia de Abajo, F. J.; Tence, M.; Henrard, L.; Taverna, D.; Pastoriza-Santos, I.; Liz-Marzan, L. M.; Colliex, C., Mapping surface plasmons on a single metallic nanoparticle. *Nat. Phys.* **2007**, *3*, 348.
(24) Kociak, M.; Stephan, O., Mapping plasmons at the nanometer scale in an electron microscope. *Chem. Soc. Rev.* **2014**, *43*, 3865.
(25) Gursoy, D.; De Carlo, F.; Xiao, X. H.; Jacobsen, C., TomoPy: a framework for the analysis of synchrotron tomographic data. *Journal of Synchrotron Radiation* **2014**, *21*, 1188.
(26) Leary, R.; Saghi, Z.; Midgley, P. A.; Holland, D. J., Compressed sensing electron tomography. *Ultramicroscopy* **2013**, *131*, 70.
(27) Nicoletti, O.; de la Pena, F.; Leary, R. K.; Holland, D. J.; Ducati, C.; Midgley, P. A., Three-dimensional imaging of localized surface plasmon resonances of metal nanoparticles. *Nature* **2013**, *502*, 80.
(28) Cherqui, C.; Thakkar, N.; Li, G. L.; Camden, J. P.; Masiello, D. J., Characterizing Localized Surface Plasmons Using Electron Energy-Loss Spectroscopy. In *Annual Review of Physical Chemistry, Vol 67*, Johnson, M. A.; Martinez, T. J., Eds. 2016; Vol. 67, pp 331.
(29) de Abajo, F. J. G.; Kociak, M., Probing the photonic local density of states with electron energy loss spectroscopy. *Phys. Rev. Lett.* **2008**, *100*.
(30) Hohenester, U.; Ditlbacher, H.; Krenn, J. R., Electron-Energy-Loss Spectra of Plasmonic Nanoparticles. *Phys. Rev. Lett.* **2009**, *103*.
(31) Mirsaleh-Kohan, N.; Iberi, V.; Simmons, P. D.; Bigelow, N. W.; Vaschillo, A.; Rowland, M. M.; Best, M. D.; Pennycook, S. J.; Masiello, D. J.; Guiton, B. S.; Camden, J. P., Single-Molecule Surface-Enhanced Raman Scattering: Can STEM/EELS Image Electromagnetic Hot Spots? *J. Phys. Chem. Lett.* **2012**, *3*, 2303.
(32) Myroshnychenko, V.; Nelayah, J.; Adamo, G.; Geuquet, N.; Rodríguez-Fernández, J.; Pastoriza-Santos, I.; MacDonald, K. F.; Henrard, L.; Liz-Marzán, L. M.; Zheludev, N. I.; Kociak, M.; García de Abajo, F. J., Plasmon Spectroscopy and Imaging of Individual Gold Nanodecahedra: A Combined Optical Microscopy, Cathodoluminescence, and Electron Energy-Loss Spectroscopy Study. *Nano Lett.* **2012**, *12*, 4172.
(33) Talebi, N.; Sigle, W.; Vogelgesang, R.; Esmann, M.; Becker, S. F.; Lienau, C.; van Aken, P. A., Excitation of Mesoscopic Plasmonic Tapers by Relativistic Electrons: Phase Matching versus Eigenmode Resonances. *ACS Nano* **2015**, *9*, 7641.
(34) Novotny, L., Effective Wavelength Scaling for Optical Antennas. *Phys. Rev. Lett.* **2007**, *98*, 266802.
(35) Bao, W.; Melli, M.; Caselli, N.; Riboli, F.; Wiersma, D. S.; Staffaroni, M.; Choo, H.; Ogletree, D. F.; Aloni, S.; Bokor, J.; Cabrini, S.; Intonti, F.; Salmeron, M. B.; Yablonovitch, E.; Schuck, P. J.; Weber-Bargioni, A., Mapping Local Charge Recombination Heterogeneity by Multidimensional Nanospectroscopic Imaging. *Science* **2012**, *338*, 1317.
(36) Paolo, B.; Jer-Shing, H.; Bert, H., Nanoantennas for visible and infrared radiation. *Rep. Prog. Phys.* **2012**, *75*, 024402.
(37) Guo, S.; Talebi, N.; Sigle, W.; Vogelgesang, R.; Richter, G.; Esmann, M.; Becker, S. F.; Lienau, C.; van Aken, P. A., Reflection and Phase Matching in Plasmonic Gold Tapers. *Nano Lett.* **2016**, *16*, 6137.

(38) Mazzucco, S.; Geuquet, N.; Ye, J.; Stéphan, O.; Van Roy, W.; Van Dorpe, P.; Henrard, L.; Kociak, M., Ultralocal Modification of Surface Plasmons Properties in Silver Nanocubes. *Nano Lett.* **2012**, *12*, 1288.
(39) Bigelow, N. W.; Vaschillo, A.; Iberi, V.; Camden, J. P.; Masiello, D. J., Characterization of the Electron- and Photon-Driven Plasmonic Excitations of Metal Nanorods. *ACS Nano* **2012**, *6*, 7497.
(40) Donoho, D. L., Compressed sensing. *IEEE Trans. Inf Theory* **2006**, *52*, 1289.
(41) Candes, E. J.; Romberg, J.; Tao, T., Robust uncertainty principles: exact signal reconstruction from highly incomplete frequency information. *IEEE Trans. Inf Theory* **2006**, *52*, 489.
(42) Lustig, M.; Donoho, D.; Pauly, J. M., Sparse MRI: The application of compressed sensing for rapid MR imaging. *Magn. Reson. Med.* **2007**, *58*, 1182.
(43) Collins, S. M.; Ringe, E.; Duchamp, M.; Saghi, Z.; Dunin-Borkowski, R. E.; Midgley, P. A., Eigenmode Tomography of Surface Charge Oscillations of Plasmonic Nanoparticles by Electron Energy Loss Spectroscopy. *ACS Photonics* **2015**, *2*, 1628.
(44) Rossouw, D.; Couillard, M.; Vickery, J.; Kumacheva, E.; Botton, G. A., Multipolar Plasmonic Resonances in Silver Nanowire Antennas Imaged with a Subnanometer Electron Probe. *Nano Lett.* **2011**, *11*, 1499.
(45) McPeak, K. M.; Jayanti, S. V.; Kress, S. J. P.; Meyer, S.; Iotti, S.; Rossinelli, A.; Norris, D. J., Plasmonic Films Can Easily Be Better: Rules and Recipes. *ACS Photonics* **2015**, *2*, 326.
(46) Klein, M.; Schwitzgebel, G., An improved lamellae drop-off technique for sharp tip preparation in scanning tunneling microscopy. *Rev. Sci. Instrum.* **1997**, *68*, 3099.
(47) Egerton, R. F.; Wang, F.; Malac, M.; Moreno, M. S.; Hofer, F., Fourier-ratio deconvolution and its Bayesian equivalent. *Micron* **2008**, *39*, 642.
(48) Bellido, E. P.; Rossouw, D.; Botton, G. A., Toward 10 meV Electron Energy-Loss Spectroscopy Resolution for Plasmonics. *Microsc. Microanal.* **2014**, *20*, 767.
(49) Fessler, J. A.; Sutton, B. P., Nonuniform fast Fourier transforms using min-max interpolation. *IEEE Trans. Sig. Process.* **2003**, *51*, 560.
(50) Buckheit, J. B.; Donoho, D. L., WaveLab and Reproducible Research. In *Wavelets and Statistics*, Antoniadis, A.; Oppenheim, G., Eds. Springer New York: New York, NY, 1995; pp 55.
(51) Hanwell, M. D.; Ayachit, U.; Muller, D. A.; Hovden, R. Tomviz: Tomographic visualization of 3D scientific data. http://www.tomviz.org/ (accessed 02/08/2017).